A Joint Illumination and Communication GaN MQW LED Model for Visible Light Communication System

DAYU SHI[1] , XUN ZHANG[1*], ZIQI LIU [1], XUANBANG CHEN [2], XIAODONG LIU [1,2], JINTAO WANG[3], JIAN SONG[3], AND ANDREI VLADIMIRESCU[4]

[1] *Institut superieur d'electronique de Paris, Paris, France*
[2] *The School of Information Engineering, Nanchang University, Nanchang, China.*
[3] *Department of Electronic Engineering, Tsinghua University, Beijing, China.*
[4] *University of California at Berkeley, Berkeley, CA, USA*
[1] *xun.zhang@isep.fr*

Abstract: This paper presents a joint illumination and communication model for Gallium Nitride (GaN) Multiple Quantum Well (MQW) Light Emitting Diodes (LEDs) used in Visible Light Communication (VLC) systems. Based on device physics, the proposed model characterizes the intrinsic nonlinearity of the LED's electro-optic conversion by incorporating the LED's material, physical structure, and bias voltage. The modeling methodology and the model's accuracy are demonstrated through experimental measurements on a commercial sample LED by a VLC system performance testbed. The validation results indicate the proposed GaN MQW LED model is consistent with physical principles and accurately predicts the LED's nonlinear impact on the VLC system under varying signal frequency and illumination intensity of the LED, underscoring its significance for analyzing and optimizing VLC systems. Overall, the proposed model offers a valuable tool for the design and optimization of VLC systems using GaN-based LEDs.

1. Introduction

Visible Light Communication (VLC) technology using Light Emitting Diodes (LEDs) modulates visible light intensity to transmit signal and simultaneously provides illumination. With advances in solid-state lighting, Gallium-Nitride (GaN) Multiple-Quantum-Well (MQW) LEDs used in VLC systems extend the bandwidth from several Megahertz (MHz) to hundreds of MHz [1–3], and improve the illumination efficacy from 135 lm/W to 235 lm/W [4]. Benefiting from joint high-speed communication and high-efficiency illumination, VLC systems become one of the most potential candidates for sixth-generation (6G) wireless communication [5–8].

In the VLC system, the LED serving for illumination and signal transmission dominates the system performance. Unfortunately, most commercial LEDs, especially widespread GaN MQW LEDs, suffer from non-linearity in both illumination and communication. They provide the highest efficiency at low injection, but as the injection increases, the efficiency droops gradually, which is the well-known phenomenon called "efficiency droop" [9]. Meanwhile, with the frequency of the input electrical signal increasing, the response of the output optical signal attenuates rapidly [10]. To accelerate the commercial acceptance of the VLC system and its integration into the existing illumination infrastructure, an accurate and generic LED model is needed from academia and industry [11, 12].

Numerous representative studies have focused on LED modeling for VLC systems. The most common LED model around 2012 was characterized as a low-pass filter, and its frequency-domain transfer function was obtained by curve fitting [13–15]. The origin of LED nonlinearity was attributed to the slow response of the phosphor coating on the LED [16]. Inspired by this notion and the low-pass filter model, several corresponding analysis and optimization approaches were subsequently explored by incorporating a blue filter to suppress the slow phosphorescent component [17–20]. Despite the experiments and demonstrations yielding effective results, a criticism of this model is the persistence of strong nonlinearity in the filtered optical signals, suggesting that the primary non-linear property of LEDs does not stem from the phosphor [21]. As such, modeling LEDs with a low-pass filter fails to characterize their intrinsic nonlinearity. VLC systems design and optimization based on this model leave space for further improvement.

The second representative LED model is proposed as the joint resistance and capacitance equivalent circuit named the "RC" equivalent circuit [22–24]. This kind of model takes into account the LED's parasitic components and models the carrier diffusion process in each layer of the LED as a differential resistance in parallel with a capacitance. Li et al. proposed a representative equivalent circuit model of the LED, along with a corresponding parameters extraction strategy [25]. The validation results of measurement curve fitting matched well the forward transfer function. Compared to the low-pass filter model, the accuracy of the "RC" equivalent circuit model was substantially enhanced. However, the fitted parameters were only valid at a specific quiescent voltage, and therefore, the characterization of the LED's illumination performance was inadequate. These shortcomings limited its applicability in practical VLC systems.

The third representative LED model was developed based on device physics. Researchers from TU Eindhoven and Signify argued that it was feasible to characterize the LED based on its internal physics processes rather than treating it as a black box using a complex generic method [26–28]. This approach reorients LED modeling towards investigating the intrinsic characteristics of LEDs from a physical perspective. Derived from the carrier rate equation to the communication performance of VLC systems, their model elucidates the origin of LED nonlinearity in relation to injection levels, significantly advancing LED modeling for VLC systems. In our view, to enhance the generality and accuracy of their model, LED communication performance should be associated with its physical parameters and illumination intensity. The current results restrict the applicability of their model to general LEDs and preclude the prediction of signal distortion when LEDs provide varying levels of illumination intensity.

In conclusion, the first and second representative LED models fail to fully characterize either the intrinsic nonlinearity caused by the material size, quantum well structure, electron polarization, or signal distortion influenced by the bias voltage. The third representative model proved that an accurate characterization of LEDs for VLC systems requires developing an LED model based on its underlying physics. However, their model cannot directly apply to a commercial LED and cannot predict the impact of LEDs on joint illumination and communication scenarios.

In this paper, we derived a GaN MQW LED model based on device physics and developed its equivalent circuit for practical applications. The model associates the LED's material and physical structure with its communication and illumination performance. The bias voltage of the LED is related to the signal response, ensuring model accuracy at high injection levels. Compared with the existing LED models, the improvements contributed by this work are summarized as follows:

- In practical VLC applications, various types, sizes, structures, and materials LEDs are selected based on system demands. Existing LED models cannot accommodate these properties as input variables. The proposed model associates the LED's material and physical structure to enhance its general applicability.

- The LED is generally biased at a large injection level in VLC systems to provide adequate brightness resulting in carrier nonlinear injection and transport. Few of the current models address that of effects. This paper considers the carrier degenerated in quantum wells due to the large injection. The proposed model employs Fermi distribution to calculate the carrier concentration to improve the model accuracy under various bias voltages.

- Few existing models clarify and accurately capture the interplay of LED's illumination and communication performance. The proposed model derives the LED's signal response associated with the bias voltage and calculates the LED's illumination intensity considering the signal magnitude to fulfill its applicability in joint illumination and communication scenarios.

The rest of the contents are structured as follows: In Sec. II, the intrinsic nonlinearity of the LED's electro-optic conversion is characterized by modeling the material and physical structure of the LED using a set of single-particle rate equations associated with the bias voltage. Sec. III illustrates the derivation of the LED equivalent circuit, which transforms the carrier equations into electrical components leading to a compact model of the GaN MQW LED. Afterward, Sec. IV presents the derivation of the LED's illumination intensity and signal response from the equivalent circuit. Meanwhile, the proposed LED model is combined with a typical VLC channel and a linear response of the VLC receiver to form a VLC transmission link model. Sec. V details the model validation. A commercial GaN MQW LED is integrated into a VLC system performance testbed as a sample LED. The measured and model-estimated VLC system performance is compared to validate the applicability and accuracy of the proposed LED model. Finally, the contributions of this paper are summarized in the conclusion remarked in Sec. VI.

2. GaN MQW LED Device Physics

2.1. Structure and energy band

A typical GaN MQW LED cross-section is depicted in Fig. 1. The LED is grown on a sapphire substrate (c-plane) using Metal-Organic Chemical Vapor Deposition (MOCVD). Along the growth direction z, a GaN buffer layer and an n-doped GaN cladding layer are successively deposited on the substrate. An InGaN layer, sandwiched between two n-type GaN layers, forms a quantum well structure. The number and thickness of quantum wells are denoted by m and L_q, respectively, resulting in an $m \times L_q$ MQW structure. A p-doped AlGaN Electron Blocking Layer (EBL) is included to prevent electron leakage before the addition of a p-doped GaN cladding layer. Negative and positive contacts are deposited on the n-type and p-type cladding layers, respectively.

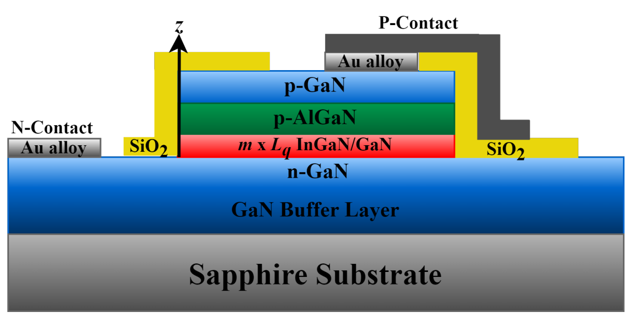

Fig. 1. Structure of a typical MQW GaN-based LED.

Based on the structure of the GaN MQW LED, the schematic energy band diagram under forward bias voltage is depicted in Fig. 2. In a joint illumination and communication scenario, the LED must transmit signals at a large bias to provide adequate brightness. Consequently, the proposed model considers three properties of the GaN MQW LED at high injection levels. Firstly, non-radiative recombination in the cladding layer and EBL cannot be ignored, as the recombination rate increases with the injection level. Secondly, the effect of leakage current

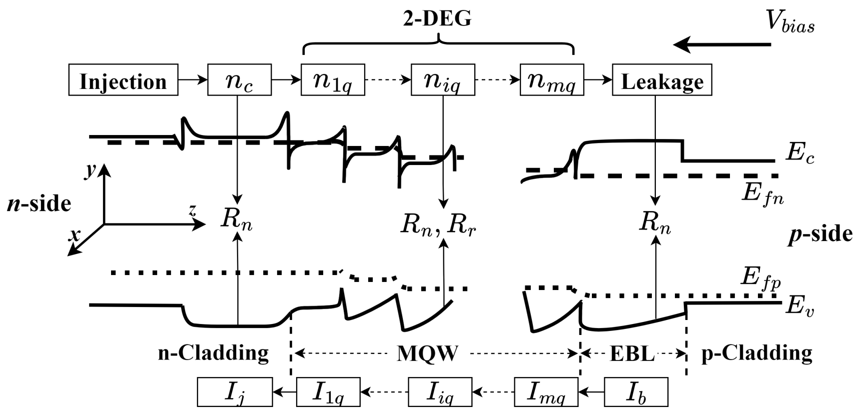

Fig. 2. Schematic energy band diagram of an MQW GaN-based LED under a forward bias voltage.

is considered, as polarization charges cause the conduction band E_c to slope upward when approaching the active region from the *n* side of the device. This shape is repeated in quantum wells, exacerbating electron leakage [29]. Lastly, electrons in quantum wells become degenerate. At high injection levels, electron concentration in quantum wells is extremely high, causing the quasi-Fermi level E_{fn} to exceed the conduction band. Consequently, the Boltzmann distribution is inapplicable, and electrons in a quantum well behave as a Two-Dimensional Electron Gas (2-DEG) [30]. Employing the effective mass approximation [31], electrons are considered quasi-free in x, y directions and quantized in the z direction.

2.2. Carriers concentration

Based on the energy band diagram, the carrier concentration in each layer of the LED is initially associated with the bias voltage. The assumptions and simplifications for calculating carrier concentrations in each layer are summarized as follows:

- The potential difference between the quasi-Fermi levels for electrons and holes is assumed identical in each layer. Therefore, the nominal voltage applied to each layer is the junction voltage V_j.
- In the *n*-type cladding layer and EBL, the non-equilibrium carriers are considered in a non-degenerate state, which is calculated by the Boltzmann distribution.
- Quantum wells are assumed to maintain local charge neutrality, where the non-equilibrium electrons concentration is equal to that of holes. Each quantum well is modeled as an infinite potential well [32] in the direction z, and a parabolic approximation is applied in the x, y direction. Coupling between adjacent wells is negligible [33].

The definitions of variables are listed in Appendix I. The non-equilibrium carriers of the *n*-type cladding layer and EBL originate from the external injection and carrier leakage. Consequently, their expression in the *n*-type cladding layer is determined by Eq. (1), and carrier leakage is calculated based on the carrier concentration in the last quantum well, n_{mq}, multiplied by the probability of carriers crossing the barrier ($V_D - V_j$), as expressed by Eq. (2).

$$n_c = n_0(\exp(\frac{qV_j}{\eta k_B T}) - 1) \tag{1}$$

$$n_b = n_{mq} \exp(-\frac{q(V_D - V_j)}{k_B T}) \tag{2}$$

In each quantum well, the non-equilibrium electrons are degenerated and considered as 2DEG. A self-consistent approach, based on the Schrödinger equation and the Poisson equation, is employed to derive the electron concentration in the quantum well [34]. The derivation is detailed in Appendix I, and the simplified electron concentration in the quantum well is given as Eq. (3). Here, the m^* represents the effective mass of the electron, and $\hbar$ is denoted as the reduced Planck constant.

$$n_q = \frac{m^* k_B T}{\pi \hbar^2 L_q} \ln(1 + \exp(\frac{E_{fn} - E_{c1}}{k_B T})) \tag{3}$$

The computation of the exponential factor $E_{fn} - E_{c1}$ is overly complex for the purpose of assessing the LED's impact on the communication system. Therefore, a polynomial fitting function, $\xi(V_j)$, is employed to fit the energy between the electron quasi-Fermi level E_{fn} and the lowest conduction band E_{c1}, as shown in Eq. (4).

$$\xi(V_j) = E_{fn}(V_j) - E_{c1}(V_j) = \alpha_1 V_j + \alpha_2 V_j^2 + \alpha_3 V_j^3 \tag{4}$$

The final simplified electron concentration in quantum wells is expressed by Eq.(5).

$$n_q(V_j) = n^* \ln(1 + \exp(\frac{\xi(V_j)}{k_B T})) \tag{5}$$

where,

$$n^* = \frac{m^* k_B T}{\pi \hbar^2 L_q} \tag{6}$$

After obtaining the analytic solutions for carrier concentrations in the n-type cladding layer, quantum wells, and the EBL as functions of the externally applied voltage, as shown in Eq. (1), (2), and (5), these expressions can be substituted into the rate equations developed in the following section to describe the carrier transport process in the LED.

2.3. Rate Equations

The single-particle rate equations methodology [35], which describes the carrier transport and recombination's physical processes, is employed to characterize the LED's intrinsic nonlinearity of the electro-optical conversion. The internal physical processes of the LED are structured as follows:

From the n side perspective shown in Fig. 2, electrons injected from the n-doped GaN cladding layer drift and diffuse into the MQW layers. Within each well, electrons partially recombine with holes, and the remainder diffuses towards the adjacent well. In the last well denoted by m, electrons cross the EBL barrier forming leakage. During the transport process, radiative recombination $\mathscr{R}r$, generating photons, occurs only in MQW layers. The non-radiative recombination $\mathscr{R}n$, comprising Auger recombination and Shockley–Read–Hall (SRH) recombination, takes place in the n-type cladding layer and quantum wells.

Several assumptions and approximations are applied to the carrier transport process:

- Carrier transport follows ambipolar diffusion, assuming both electrons and holes diffuse in a coupled manner [36]. The transport process of holes can be represented by that of electrons.

- The process of electrons captured and released from quantum wells is negligible in our model due to its associated time of only hundreds of picoseconds [37], which is much shorter than the LED's response time.
- Interfacial recombination and recombination occurring during carrier crossing of barriers are neglected because these processes are overly complex and insignificant for communication system analysis.

Based on the above assumptions and approximations, the rate equations describing the LED's internal physical processes are expressed in Eq. (7) to (11).

$$\frac{dn_c}{dt} = \frac{I_j - I_{1q}}{qA_cL_c} - \mathscr{R}_n(n_c) \tag{7}$$

$$\frac{dn_{1q}}{dt} = \frac{I_{1q} - I_{2q}}{qA_qL_q} - \mathscr{R}_{1qn}(n_{1q}) - \mathscr{R}_{1qr}(n_{1q}) \tag{8}$$

$$\frac{dn_{iq}}{dt} = \frac{I_{iq} - I_{(i+1)q}}{qA_qL_q} - \mathscr{R}_{iqn}(n_{iq}) - \mathscr{R}_{iqr}(n_{iq}) \tag{9}$$

$$\frac{dn_{mq}}{dt} = \frac{I_{mq} - I_b}{qA_qL_q} - \mathscr{R}_{mqn}(n_{mq}) - \mathscr{R}_{mqr}(n_{mq}) \tag{10}$$

$$\frac{ds}{dt} = \sum_{i=1}^{m} \beta_{sp}\mathscr{R}_{iqr}(n_{iq}) - \frac{s}{\tau_{ph}} \tag{11}$$

The variables in the n-type cladding layer, quantum wells, and EBL are distinguished by the subscripts c, q, and b, respectively. I_j represents the current injected into the LED from the n-type cladding layer. The subscript iq denotes the variables of the i-th quantum well from the n side to the p side. Eq. (7) to (10) illustrate the dynamic equilibrium of electrons in each layer. The rate of electron non-equilibrium concentration change equals the net injected electrons minus the recombination rate. Eq. (11) describes that the rate of change in photons density equals the total photons generated from each quantum well minus the photons lost to absorption. The Shockley diode equation [38], expressed by Eq. (12), is used to describe the relationship between the junction voltage V_j and injected current I_j of the LED. The leakage current I_b is calculated by the quantity of charge in the EBL divided by the effective space transport time [39], as shown in Eq. (13).

$$I_j = I_s(\exp(\frac{qV_j}{\eta k_B T}) - 1) \tag{12}$$

$$I_b = \frac{qA_bL_bn_b}{\tau_b} \tag{13}$$

The radiative and non-radiative recombination rate ($\mathscr{R}_r$ and $\mathscr{R}_n$) are determined based on the well-known ABC model [40] which uses a third-order polynomial equation to represent the recombination rate.

$$\mathscr{R}_r = \gamma_2 n^2 \tag{14}$$

$$\mathscr{R}_n = \gamma_1 n + \gamma_3 n^3 \tag{15}$$

The first and third-order terms represent the non-radiative recombination, which consists of the SRH and Auger recombination. The second-order term represents radiative recombination.

To distinguish them from other parameters, γ_1, γ_2, and γ_3 are used as coefficients for the first, second, and third orders of the polynomial, respectively. The coefficients are considered constant in each layer.

Eq. (7) to (15) illustrate the carrier transport process from injection to leakage. By substituting the analytical solution of carrier concentration, the physical parameters and the bias voltage of the LED are correlated with the rate equations. From the above analysis, the equivalent circuit of the GaN MQW LED can be developed.

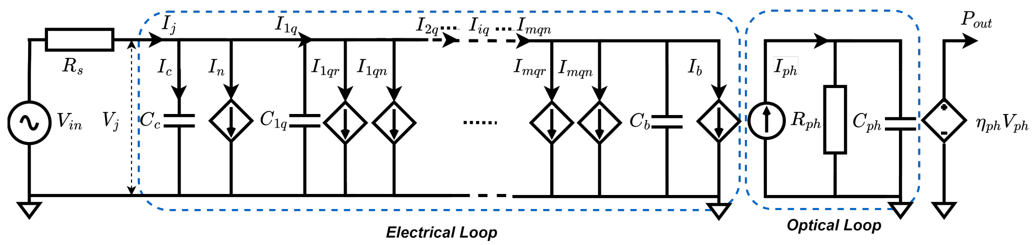

Fig. 3. The equivalent circuit of GaN MQW LED.

3. Equivalent Circuit of GaN MQW LED

To incorporate the physical behavior of the GaN MQW LED in VLC systems, an equivalent electrical circuit is developed based on the derivations from the previous section. The rate equations describing electron transport and photon generation are transformed into an electrical loop and an optical loop, respectively. By associating the output light power of the LED with the input voltage and current, the electro-optical conversion process is represented by the circuit shown in Fig. 3. The derivation of this circuit is detailed below.

3.1. Electrical Loop

Setting the junction voltage as V_j, the rate equation and the corresponding carrier concentration describing the n-type cladding layer are represented in Eq. (16) and (17). For expressing I_j, the rate equation is multiplied by qA_cL_c on both sides, and $\frac{dn_c}{dt}$ is decomposed by $\frac{dn_c}{dV_j} \cdot \frac{dV_j}{dt}$ resulting in Eq. (18).

$$\frac{dn_c}{dt} = \frac{I_j - I_{1q}}{qA_cL_c} - \mathscr{R}_n(n_c) \tag{16}$$

$$n_c = n_0(\exp(\frac{qV_j}{\eta k_B T}) - 1) \tag{17}$$

$$I_j = qA_cL_c\frac{dn_c}{dV_j} \cdot \frac{dV_j}{dt} + I_{1q} + qA_cL_c\mathscr{R}_n(n_c) \tag{18}$$

where,

$$\frac{dn_c}{dV_j} = \frac{qn_0}{\eta k_B T}\exp(\frac{qV_j}{\eta k_B T}) \tag{19}$$

Substituting the differential of carrier concentration (Eq. (19)) into the decomposed rate equation (Eq. (18)) and defining the coefficient of the term $\frac{dV}{dt}$ as C_c, the transformed circuit equation for the n-type cladding layer is established in Eq. (20).

$$I_j = C_c \frac{dV_j}{dt} + I_{1q} + I_n \tag{20}$$

where,

$$I_n = qA_cL_c\mathscr{R}_n(n_c) = qA_cL_c(\gamma_1 n_c + \gamma_3 n_c^3) \tag{21}$$

$$C_c = \frac{q^2 n_0 A_c L_c}{\eta k_B T}\exp(\frac{qV_j}{\eta k_B T}) \tag{22}$$

In this case, the circuit equation represents the injected current is equal to the current of an equivalent voltage-controlled capacitance, plus the non-radiative current and the current flowing into the first quantum well, which corresponds to the physical process of the LED. Additionally, the units of C_c and I_n are C/V and C/s, respectively, aligning with their physical meanings. By applying the same methodology to the m quantum wells, the remaining carrier rate equations (Eq. (8) to (10)) are transformed into circuit equations as shown in Eq. (23) to (25).

$$I_{1q} = C_{1q}\frac{dV_j}{dt} + I_{2q} + I_{1qn} + I_{1qr} \tag{23}$$

$$I_{iq} = C_{iq}\frac{dV_j}{dt} + I_{(i+1)q} + I_{iqn} + I_{iqr} \tag{24}$$

$$I_{mq} = C_{mq}\frac{dV_j}{dt} + I_b + I_{mqr} + I_{mqn} \tag{25}$$

Moreover, the voltage-controlled capacitance C_{iq}, recombination components(I_{iqr} and I_{iqn}) and leakage I_b are expressed as Eq. (26) to (29).

$$C_{iq} = \frac{qA_qL_qn^* \exp(\frac{\xi(V_j)}{k_BT})}{k_BT(1+\exp(\frac{\xi(V_j)}{k_BT}))}\cdot(\alpha_1 + 2\alpha_2 V_j + 3\alpha_3 V_j^2) \tag{26}$$

$$I_{iqr} = qA_qL_q\mathscr{R}_{iqr}(n_{iq}) = qA_qL_q(\gamma_2 n_{iq}^2) \tag{27}$$

$$I_{iqn} = qA_qL_q\mathscr{R}_{iqr}(n_{iq}) = qA_qL_q(\gamma_1 n_{iq} + \gamma_3 n_{iq}^3) \tag{28}$$

$$\begin{aligned} I_b &= \frac{qA_bL_b}{\tau_b} n_{mq}\exp(-\frac{q(V_D - V_j)}{k_BT}) \\ &= \frac{qA_bL_b}{\tau_b}\cdot n^* \ln(1+\exp(\frac{\xi(V_j)}{k_BT}))\cdot\exp(-\frac{q(V_D-V_j)}{k_BT}) \end{aligned} \tag{29}$$

3.2. Optical Loop

The photonic rate equation Eq. (11) describes the relationship of the radiative recombination current generating photons. It is multiplied by qA_qL_q on both sides of the equation, formulated in Eq. (30). We define the photon voltage V_{ph}, photon capacitance C_{ph}, and photon resistance R_{ph} as $V_{ph} = sA_qL_qV_{th}$, $C_{ph} = q/V_{th}$, and $R_{ph} = V_{th}\tau_{ph}/q$, respectively. Here, V_{th} represents the thermal voltage given by $V_{th} = k_BT/q$. While the radiative recombination rate $\mathscr{R}_{iqr}$ multiplied by qA_qL_q just right equals to the radiative recombination current I_{iq}. Multiplying the spontaneous emission coefficient β_{sp} with the sum of I_{iq}, the photonic current can be expressed as Eq. (31).

$$\frac{ds}{dt} \cdot qA_q L_q = \sum_{i=1}^{m} \beta_{sp} \mathscr{R}_{iqr}(n_{iq}) \cdot qA_q L_q - \frac{s \cdot qA_q L_q}{\tau_{ph}} \tag{30}$$

$$I_{ph} = \sum_{i=1}^{m} \beta_{sp} I_{iqr}(n_{iq}) = C_{ph} \frac{dV_{ph}}{dt} + \frac{V_{ph}}{R_{ph}} \tag{31}$$

In the proposed model, the barrier capacitance C_b, situated between the last quantum well m and EBL, and the parasitic resistance R_s located at contact are considered. The impact of parasitic inductance and capacitance is negligible for a device operating within a bandwidth of several MHz. With the effective barrier area A_{eff} approximation [41], the barrier capacitance is determined by Eq. (32).

$$C_b = A_{eff} \left[\frac{q\epsilon_{mq}\epsilon_b N_A N_D}{2(\epsilon_{mq} N_D + \epsilon_b N_A)} \frac{1}{V_D - V_j} \right]^{\frac{1}{2}} \tag{32}$$

3.3. Output of the equivalent circuit

Based on the above transformation of rate equations in each layer, the carrier transport and photon generation process in LED are equivalent to the current functions of the electrical and optical loops, respectively described by Eq. (33) and (34).

$$I_j = C_c \frac{dV_j}{dt} + \sum_{i=1}^{m} (C_{iq} \frac{dV_j}{dt} + I_{iqr} + I_{iqn}) + I_b \tag{33}$$

$$I_{ph} = \sum_{i=1}^{m} \beta_{sp} I_{iqr}(n_{iq}) = C_{ph} \frac{dV_{ph}}{dt} + \frac{V_{ph}}{R_{ph}} \tag{34}$$

In our model, the output light power P_{out} of the LED is considered proportional to the photonic density s. Because VLC systems are achieved by Intensity Modulated/Direct Detection (IM/DD) mechanism [42]. the detailed derivation of the optical spectrum in [43] is insignificant. A coefficient η_{ph} is defined as the light extraction rate to describe the relationship between the output light power (P_{out} in Watt) of the LED and the photon voltage V_{ph}.

$$P_{out}(\text{Watt}) \propto s \tag{35}$$

$$P_{out}(\text{Watt}) = \eta_{ph} V_{ph} \tag{36}$$

Combining Eq. (33) and (34) with the output power of the LED Eq. (36), the GaN MQW LED equivalent circuit is established as Fig. 3. Based on the equivalent circuit, the illumination intensity and communication performance are derived from the Direct Current (DC) and small signal analysis in the next section.

4. Illumination intensity and Signal Response of GaN MQW LED

In a joint communication and illumination scenario, the LED is operated under a large forward bias to provide sufficient light for illumination, and an electric signal is imposed on the bias to generate the optical signal for communication. Considering the amplitude of the electric signal is generally much smaller than that of the bias and the applicability of the proposed model to practical VLC systems, the signal response of the LED is derived from a small signal analysis. Consequently, the LED's illumination intensity is composed of the output signal power and illumination power driven by the bias voltage.

4.1. Illumination intensity

The illumination intensity in our model is quantified in Lux (lx) [44], which measures the level of light detected by the human eye. The relationship between Watt and Lux is established in Eq. (37), with η_L and A_{rec} representing the efficacy (lm/W) of the LED and the area of the detector, respectively.

$$P_L(\text{Lux}) = \frac{P(Watt) \cdot \eta_L}{A_{rec}} \tag{37}$$

To compute the illumination power driven by the bias voltage (P_L), a DC analysis is performed on the equivalent circuit. After the LED's bias voltage V_{in} is set, the junction voltage V_j remains constant, rendering $\frac{dV}{dt}$ at zero the barrier capacitance as an open circuit. The total illumination intensity of the LED (P_{out}) is expressed as Eq. (38).

$$P_{out}(\text{Lux}) = P_L + p_{out}(t) \tag{38}$$

where, $p_{out}(t)$ represents the LED's output signal power. The junction voltage V_j, the photon voltage V_{ph}, and the radiative current I_{iqr} are expressed in Eq. (39) to (41), respectively. The illumination power driven by the bias voltage is derived as Eq. (42).

$$V_j = V_{in} - I_j R_s \tag{39}$$

$$V_{ph} = R_{ph} \sum_{i=1}^{m} \beta_{sp} I_{iqr}(n_{iq}) \tag{40}$$

$$I_{iqr} = qA_q L_q \mathscr{R}_{iqr}(n_{iq}) = qA_q L_q(\gamma_2 n_{iq}^2) \tag{41}$$

$$\begin{aligned} P_L &= \frac{\eta_L \eta_{ph} R_{ph}}{A_{rec}} \cdot \sum_{i=1}^{m} \beta_{sp} q A_q L_q \gamma_2 n_{iq}^2 \\ &= \frac{\eta_L \eta_{ph} R_{ph}}{A_{rec}} \cdot \sum_{i=1}^{m} \beta_{sp} q A_q L_q \gamma_2 \cdot [n^* \ln(1 + \exp(\frac{\xi_{iq}(V_{in} - I_j R_s)}{k_B T}))]^2 \end{aligned} \tag{42}$$

4.2. Signal Response of GaN MQW LED

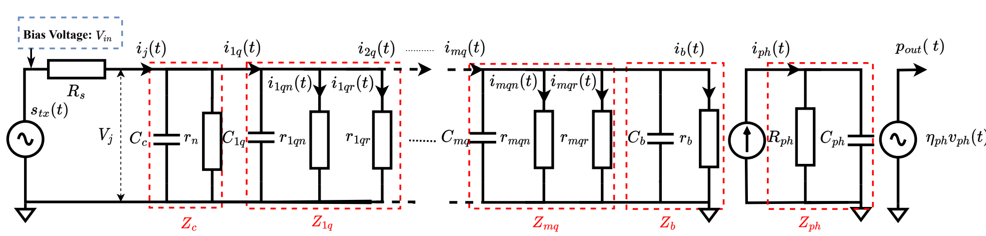

Fig. 4. The small-signal equivalent circuit of GaN MQW LED.

The signal response of the GaN MQW LED is derived through a small-signal analysis. Fig. 4 illustrates the small-signal equivalent circuit model of the LED. The small-signal components are differentiated by the use of lowercase symbols. The bias voltage applied to the small-signal equivalent circuit is supposed as V_{in}, while the quiescent junction voltage is symbolized as V_j. Proceeding from the presumed quiescent point of the small-signal equivalent circuit, the impulse response of the LED h_{led} describing the relationship between the input signal $s_{tx}(t)$ and the power of the output optical signal $p_{out}(t)$ is derived in the following.

All voltage-controlled current sources in the previous equivalent circuit, shown in the Fig. 3, are equivalent to the small signal resistances under the supposed quiescent junction voltage V_j, denoted by r_n, r_{iqr}, r_{iqn}, and r_b and expressed in Eq. (43) to (46).

$$\frac{1}{r_n} = \left.\frac{dI_n}{dV}\right|_{V=V_j} = qA_cL_cN_c(\gamma_1 + 3\gamma_3 \cdot n_c^2) \tag{43}$$

$$\frac{1}{r_{iqr}} = \left.\frac{dI_{iqr}}{dV}\right|_{V=V_j} = 2qA_qL_qN_{iq} \cdot \gamma_2 \cdot n_{iq} \tag{44}$$

$$\frac{1}{r_{iqn}} = \left.\frac{dI_{iqn}}{dV}\right|_{V=V_j} = qA_qL_qN_{iq}(\gamma_1 + 3 \cdot \gamma_3 n_{iq}^2) \tag{45}$$

$$\frac{1}{r_b} = \left.\frac{dI_b}{dV}\right|_{V=V_j} = \frac{qA_bL_b}{\tau_b}N_b \tag{46}$$

where, N_c, N_{iq}, and N_b represent the differential of non-equilibrium carrier concentration in each layer derived as Eq. (47) to (49).

$$N_c = \left.\frac{dn_c}{dV}\right|_{V=V_j} = \frac{qn_0}{\eta k_BT}\exp(\frac{qV_j}{\eta k_BT}) \tag{47}$$

$$N_{iq} = \left.\frac{dn_{iq}}{dV}\right|_{V=V_j} = \frac{n^*\exp(\frac{\xi(V_j)}{k_BT})}{k_BT(1+\exp(\frac{\xi(V_j)}{k_BT}))} \cdot (\alpha_1 + 2\alpha_2V_j + 3\alpha_3(V_j)^2) \tag{48}$$

$$N_b = \left.\frac{dn_b}{dV}\right|_{V=V_j} = N_{mq}\exp(\frac{q(V_j - V_D)}{k_BT}) + \frac{qn_{mq}}{k_BT}\exp(\frac{q(V_j - V_D)}{k_BT}) \tag{49}$$

All voltage-controlled capacitances, denoted by C_c, C_{1q}, ..., C_{mq}, and C_b, are calculated by substituting the quiescent junction voltage V_j, as detailed in the previous section, in accordance with Eq. (22), (26), and (32). To provide a clear representation, the small signal equivalent circuit is segmented into different parts based on the layer of the LED. The impedance of n-type cladding layer, quantum well, and EBL are assigned as Z_c, Z_{iq}, and Z_b respectively, which are further summed up to calculate the impedance of the electrical loop indicated by Z_E. The photonic loop's impedance is expressed as Z_{ph}, which comprises photon resistance and capacitance. Considering the impedance of the signal source Z_s, we derive the transfer function of GaN MQW LED in units of (Watt/V) as shown in Eq. (56).

$$Z_c = \frac{r_n}{1 + j\omega C_cr_n} \tag{50}$$

$$Z_{iq} = \frac{r_{iqr}r_{iqn}}{r_{iqr} + r_{iqn} + j\omega r_{iqr}r_{iqn}C_{iq}} \tag{51}$$

$$Z_b = \frac{r_b}{1 + j\omega C_br_b} \tag{52}$$

$$Z_E = (\frac{1}{Z_c} + \frac{1}{Z_b} + \sum_{i=1}^{m}\frac{1}{Z_{iq}})^{-1} \tag{53}$$

$$Z_{ph} = \frac{R_{ph}}{1 + j\omega R_{ph}C} \tag{54}$$

$$p_{out}(j\omega) = s_{tx}(j\omega) \cdot \frac{\eta_{ph}\beta_{sp}Z_E Z_{ph}}{Z_E + R_s + Z_s} \cdot \sum_{i=1}^{m} \frac{1}{r_{iqr}} \tag{55}$$

$$H_{led}(V_{in}, j\omega) = \frac{p_{out}(j\omega)}{s_{tx}(j\omega)} = \frac{\eta_{ph}\beta_{sp}Z_E Z_{ph}}{Z_E + R_s + Z_s} \cdot \sum_{i=1}^{m} \frac{1}{r_{iqr}} \tag{56}$$

To obtain the transfer function of GaN MQW LED in a real-time communication system, the impulse response is derived by employing an inverse Fourier Transform shown in Eq. (57).

$$h_{led}(V_{in}, t) = \mathcal{F}^{-1}(H_{led}(V_{in}, j\omega)) = \frac{1}{2\pi}\int_{-\infty}^{\infty} \frac{\eta_{ph}\beta_{sp}Z_E Z_{ph}}{Z_E + R_s + Z_s} \cdot \sum_{i=1}^{m} \frac{1}{r_{iqr}} \cdot e^{-j\omega t} d\omega \tag{57}$$

4.3. VLC Transmission Link Model

To assess the applicability of the proposed model integration into practical VLC systems, a typical VLC channel model and a linear response of a VLC receiver are united with the LED model forming a basic VLC transmission link model. In this paper, the Non-Line-of-Sight (NLoS) propagation is ignored, and the VLC receiver is considered comprising of an Avalanche Photodiode (APD) and a Transimpedance Amplifier (TIA).

Lambertian radiation relationship, employed as a channel model in most VLC research [20], is expressed in Eq. (58). In this model, the time delay of light propagation is negligible due to the transmission distance being far smaller than the light speed.

$$h_c(D, \psi, \theta, t) = \delta(t) \cdot \frac{(\mu + 1) * A_{rec} * cos(\psi)^{\mu} * cos(\theta)}{2\pi D^2} \tag{58}$$

$$\mu = \frac{-\ln 2}{\ln \cos \Phi_{1/2}} \tag{59}$$

where, θ, ψ, $\Phi_{1/2}$ are the angle of transmission direction, angle of receiving direction, and semi-angle at half-power of the LED. μ and D are the order of Lambertian radiation and distance between LED and APD, respectively.

According to the modulation bandwidth and frequency response flatness of APDs are much better than that of the LED [45]. The response of the VLC receiver is calculated as the gain of TIA G_{am} (V/A), multiplying the integral of the photo-sensitivity κ (A/W) on the optical spectrum. Assuming the maximum and the minimum wavelength emitted by the LED as λ_{max} and λ_{min}, the response of the receiver in units of (V/Watt) is expressed as Eq. (60).

$$h_{rx}(\lambda_{min,max}, t) = \delta(t) G_{am} \int_{\lambda_{min}}^{\lambda_{max}} \kappa(\lambda) d\lambda \tag{60}$$

The time response model of the VLC transmission link is derived in unite of (V/V) by convolution (denoted by $\otimes$) our proposed GaN MQW LED model with the channel and receiver model, and adding a random noise σ_n, shown in Eq. (61).

$$h_{vlc}(V_{in}, t, D, \psi, \theta, \lambda_{min,max}, t) = h_{led}(V_{in}, t) \otimes h_c(D, \psi, \theta, t) \otimes h_{rx}(\lambda_{min,max}, t) + \sigma_n \tag{61}$$

The IM/DD property of VLC systems requires a real value for the electrical signal as an input. For any modulated complex signal, an In-Phase and Quadrature (IQ) modulation is applied to transform the complex signal into real with the central frequency ω_c. A transmitted signal $s_{tx}(t)$ and the IQ modulation denoted by $\mathbb{M}$ are expressed as Eq. (62) and (63).

$$s_{tx}(t) = a(t) + jb(t) \tag{62}$$

$$\mathbb{M}(s_{tx}(t), \omega_c) = a(t) \cdot cos(\omega_c t) - b(t) \cdot sin(\omega_c t) \tag{63}$$

where, $a(t)$ and $b(t)$ are the real and imaginary signal, respectively. The received signal ($s_{rx}(t)$) from the VLC transmission link and the total illumination intensity provided by the LED (P_{out}) are expressed as Eq. (64) and (65).

$$s_{rx}(t) = h_{vlc}(V_{in}, t, D, \psi, \theta, \lambda_{min,max}, t) \otimes \mathbb{M}(s_{tx}(t), \omega_c) \tag{64}$$

$$P_{out}(V_{in}, s_{tx}, t) = P_L + \frac{\eta_L s_{tx}(t) \otimes h_{led}(V_{in}, t)}{A_{rec}} \tag{65}$$

Table 1. The Parameters of the Validation

Material Parameters of the Sample LED.			
* Collection from References [46,47]; $^+$ Setting from typical value range			
Definition	Symbol	Value	Unite
$^+$Transection area of cladding layer, quantum well and EBL	$A_{c,q,b}$	1×10^{-8}	cm^2
*Spontaneous emission coefficient	β_{sp}	1×10^{-4}	cm^2
*Dielectric constant	ϵ_0	8.85×10^{-12}	F/m
*Relative dielectric constant of InGaN	ϵ_r	10.2	eV
*Semi-angle at half power of LED	Φ	60	$^\circ$
*Reduced Plank constant	$\hbar$	1.05×10^{-34}	$J \cdot s$
*Boltzmann constant	k_B	1.38×10^{-23}	J/K
$^+$Thickness of cladding layer	L_c	5×10^{-5}	cm
$^+$Thickness of quantum well	L_q	1.5×10^{-6}	cm
$^+$Thickness of EBL	L_b	6×10^{-6}	cm
$^+$Number of quantum well	m	3	
*Mass of electron	m_0	9.11×10^{-31}	kg
*Effective mass of electrons in perpendiculars direction(GaN)	$m_\perp^*$	$0.2 \cdot m_0$	kg
$^+$Efficacy of LED	η_L	100	lm/W
*Elementary charge	q	1.6×10^{-19}	C
$^+$Temperature	T	300	K
$^+$Photons lifetime	τ_{ph}	1×10^{-13}	s
*Thermal voltage	V_{th}	0.026	V
Parameters of Channel and Transceiver			
*Effective area of photo-receiver	A_{rec}	1.96×10^{-3}	cm^2
$^+$Distance between LED and receiver	D	10	cm
$^+$Semi-angle at half power of LED	Φ	45	$^\circ$
$^+$Transceiver angle	ψ, θ	0	$^\circ$
*Gain of TIA	G_{am}	20	dB
*Load resistance of receiver	R_{load}	50	Ω
*Output impedance of signal source	Z_s	50	Ω

5. Experimental Validation

A commercial white LED, comprising an InGaN/GaN blue LED chip and a Yttrium Aluminum Garnet (YAG) phosphor, serves as a sample to validate the proposed GaN MQW LED model. The LED chip features a three-quantum-well structure similar to the theoretical model shown in Fig. 1. The parameters of the LED's materials and the transceiver circuits are obtained from references and datasheets remarked by * in Tab 1. The parameters absent from the datasheet are set from their typical value ranges, denoted by $^+$. The influence of the phosphor is temporarily replaced by constant attenuation and delay during light extraction from the LED chip. The proposed GaN MQW LED model is validated by comparing the consistency between the model prediction and the sample LED's measurement. Among the validation, the model's precision in characterizing the LED's non-linear impact on (i) device performance; (ii) transmitted signal; and (iii) joint illumination and communication VLC system performance are evaluated to verify its functionality for VLC system design and optimization. The setup of the validations is outlined below.

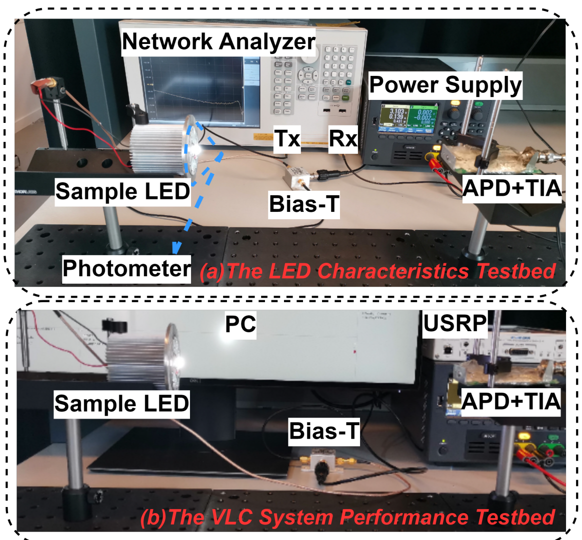

Fig. 5. Experimental setup: (a) The LED device characteristics testbed. (b) The VLC system performance testbed.

5.1. Validation setup

Among the assessment of LED's nonlinear impact, the sample LED is integrated into an LED device characteristics testbed and a VLC system performance testbed for measurement, shown in Fig. 5. The emulation process of the proposed model is depicted in Fig. 6. During the measurement, the noise floor σ_m of the VLC transmission link is recorded and applied to the model estimated signal $s_{rx}^{est}(t)$ to ensure the emulation at the same noise level as the measurements.

First, the proposed model characterizing LED's nonlinear impact on device performance is validated by fitting the model to the measurements obtained from the sample LED depicted in Fig. 5 (a). A KEYSIGHT E5061B network analyzer generates a signal swept over frequency transmitted over the VLC transmission link, which contains a Bias-T, the sample LED, the optical wireless channel, an APD, and a TIA, to calculate the power transfer function (S_{21}). Substituting all the known parameters, the LED's power transfer function could be fitted. Meanwhile, an accurate voltage and current source, KEYSIGHT E36234, serving as the power supply, records the bias voltage and the injected current. Additionally, a photometer is put next to the LED to measure the output illumination intensity on each bias voltage. The electro-optical conversion property is fitted by the bias voltage, injected current, and output illumination intensity.

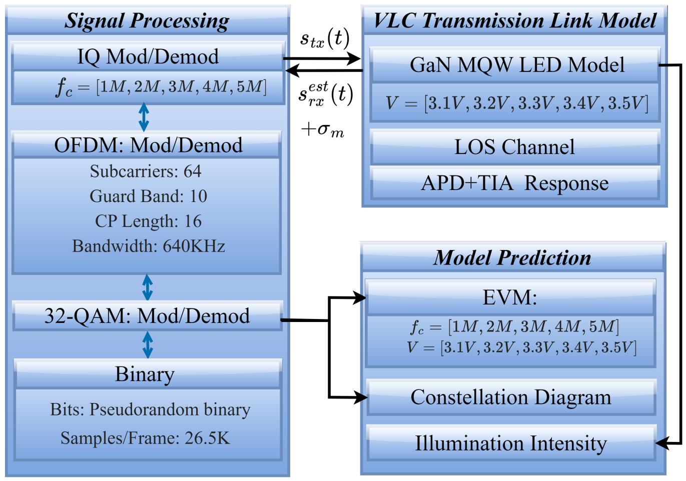

Fig. 6. The emulation process of the proposed model.

Second, the model characterizing the LED's nonlinear impact on the transmitted signal is validated by the VLC system performance testbed, shown in Fig. 5 (b). A 32-Quadrature Amplitude Modulation (QAM) Orthogonal Frequency Division Multiplexing (OFDM) signal generated in a Personal Computer (PC) is sent to the Universal Software Radio Peripheral (USRP) by the GNU Radio framework to transform the digital signal into an analog signal [48]. The transformed analog signal passed through the VLC transmission link and was collected back to demodulate and draw the constellation diagram. During the measurement, all components except the sample LED were guaranteed in a linear working range to avoid amplitude and phase distortion. The channel attenuation was measured and compensated on the received signal. Thus, the shifting of the constellation diagram almost entirely reflects the LED's nonlinear impact on the transmitted signal. Fig. 6 illustrates the process of the proposed model emulating the measurement in MATLAB. The noise floor during the measurement is recorded and applied to the model estimated signal $s_{rx}^{est}(t)$ to ensure the emulation at the same noise level as the measurements. Employing MATLAB emulation, the model estimated constellation diagram is generated. To emphasize the significance of the proposed LED model, a conventional Additive White Gaussian Noise (AWGN) model, used in most VLC research to represent the LED nonlinearity, replaces the proposed GaN MQW LED model in the emulation, forming a control group. Comparing the measured, our LED model estimated, and the AWGN model estimated constellation diagrams reflects the proposed model's performance.

Thirdly, considering the dual functionality of the VLC system, illumination and communication, the proposed model reflecting the LED's nonlinear impact on VLC system performance is validated in a practical joint illumination and communication scenario. Employing the same method of measurement and emulation as the previous validation, shown in Fig. 5(b) and Fig. 6, where the center frequency f_c of the input signal was swept to cover general commercial LED's bandwidth, and the bias voltage V was varied to generate a practical indoor illumination intensity [49]. The Error Vector Magnitudes (EVM) of the signal transmission, employed as the indicator of system performance, are calculated from measurement and model estimation. The comparison of the error between them indicates the validation result.

5.2. The LED Device Performance

Table 2. Fitted and Calculated Parameters.

Fitted Parameters	Values	Calculated Parameters	Values
α_1	-10.45	$C_c\|_{V=3.1-3.5}$	$\{4.54nF, 7.12nF, 9.94nF, 13.60nF, 17.22nF\}$
α_2	4.10		
α_3	0	$C_q\|_{V=3.1-3.5}$	$\{5.41nF, 7.95nF, 10.70nF, 14.30nF, 17.87nF\}$
γ_1	6×10^{9}		
γ_2	3×10^{-15}	$r_n\|_{V=3.1-3.5}$	$\{34.51\Omega, 20.20\Omega, 12.80\Omega, 7.75\Omega, 5.01\Omega\}$
γ_3	6×10^{-38}		
η	3.07	$r_{qn}\|_{V=3.1-3.5}$	$\{0.33\Omega, 0.18\Omega, 0.11\Omega, 0.07\Omega, 0.05\Omega\}$
I_s	$3\times10^{-17}\,A$		
R_s	$1.56\,\Omega$	$r_{qr}\|_{V=3.1-3.5}$	$\{0.55\Omega, 0.33\Omega, 0.23\Omega, 0.16\Omega, 0.12\Omega\}$
V_D	$3.3\,V$		
$\zeta_1\cdot\eta_{ph}$	0.16	$r_b\|_{V=3.1-3.5}$	$\{357.21\Omega, 68.26\Omega, 19.71\Omega, 6.03\Omega, 2.45\Omega\}$
$\zeta_2\cdot C_b\|_{V=3.1-3.5}$	$\{479.22nF, 869.02nF, 1.15\mu F, 1.44\mu F, 1.93\mu F\}$	R_{ph}	$16.25K$
$P_{nlos}\|_{V=3.1-3.5}$	$\{15dB, 14dB, 12dB, 10dB, 9dB\}$	C_{ph}	$6aF$

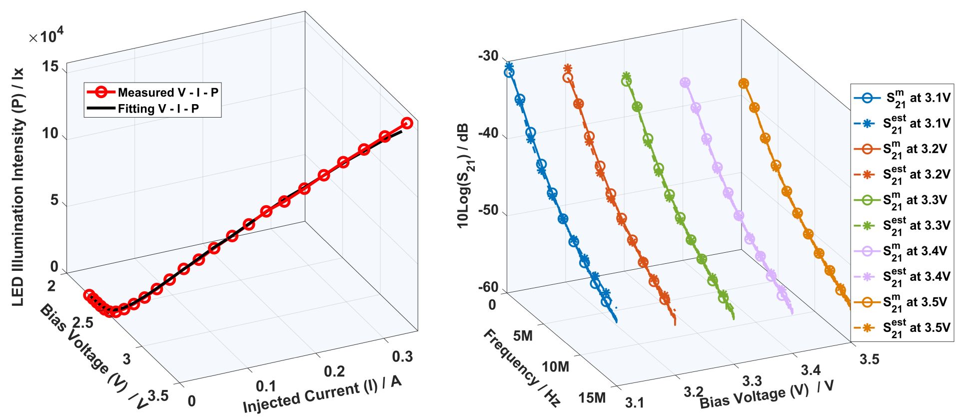

Fig. 7. The fitting results: (a) The bias voltage (V), injected current (I), and output illuminance(P) of the LED. (b) The LED's S_{21} at the applied voltage from 3.1V to 3.5V.

The model's parameters, tied to the material and physical structure of the LED, are calculated from references of the sample LED depicted in the right section of Tab. 2. Parameters arising from simplifying the LED's physical processes are fitted from the measurements shown on the left side of Tab. 2. The fitting results of the DC characteristics and the power transfer function are shown in Fig. 7 (a) and Fig. 7 (b), respectively. the attenuation and delay effects of YAG phosphorus are provisionally represented by multiplying factors ζ_1 and ζ_2 with the light extraction rate η_{ph} and the barrier capacitance C_b, respectively. The channel is solely calculated for the LoS propagation, while the NLoS transmission is adjusted as a constant compensation P_{nlos}.

According to the fitted and calculated parameters listed in Tab. 2, the diffusion capacitance in the cladding layer C_c, quantum well C_q, and EBL $\zeta_2\cdot C_b$ escalates in relation to the injection level due to the increasing charge amount, consistent with physical principles. The non-radiative recombination resistance in the cladding layer r_n is two orders of magnitude higher than that in the quantum well, indicating that the recombination current is primarily concentrated in the quantum well. This observation aligns with the theoretical distribution of carrier concentration within the LED. When comparing the radiative and non-radiative recombination resistances in the quantum well (r_{qn}, r_{qr}) and the barrier resistance (r_b), r_{qn} and r_b decrease at a much faster rate than r_{qr}. This outcome suggests an increased proportion of non-radiative current and leakage current in the total current, concomitant with the injection level. This phenomenon is characteristic of the GaN MQW LED, known as efficiency droop. Consequently, the derived model adheres to physical principles and accurately mirrors well-known physical phenomena.

The fitting results for the DC characteristics of the LED are depicted in Fig. 7 (a). It is evident that the proposed model accurately represents the relationship between the LED's bias voltage (V), injected current (I), and illumination intensity (P). Minor fitting discrepancies at high injection levels are attributed to the diminishing accuracy of the photometer during measurements. Fig. 7 (b) presents the fitting outcomes for the LED's power transfer function (S_{21}) under varying bias voltages. The power transfer function demonstrates a decline as the bias voltage increases. The errors at low bias voltages are higher than those at higher voltages, presumably due to the approximation of the model. At low injection level, ignoring the interfacial state effects [50] and quantum wells coupling leads to slightly inaccurate carrier concentration influences the estimation results.

5.3. Impact of LED's Nonlinearity on Transmitted Signal

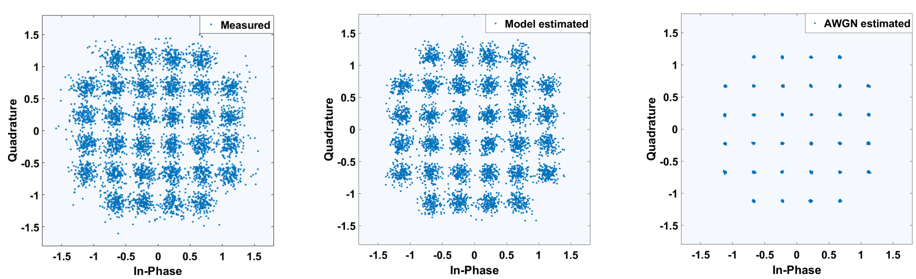

(a) (b) (c)

Fig. 8. Constellation diagram of received 32-QAM OFDM signal at central frequency f_c=3MHz, bias voltage V=3.1V: (a) Measured. (b) Proposed model estimated. (c) AWGN model estimated.

The estimated and measured constellation diagrams of the received signals at 3.1V bias and 3MHz central frequency are displayed in Fig. 8. The measured constellation diagram indicates visually in Fig. 8 (a) that the signal transmission through the VLC system is distorted by the LED's nonlinearity even though the signal frequency and power operate within a linear working range. Fig. 8 (b) reflects the distortion from the LED's nonlinearity can be predicted by the proposed model. However, in the same emulation setup, employing the AWGN model to represent LED's nonlinearity, as most VLC research applied, cannot predict such huge distortion from the LED, shown in Fig. 8 (c). The comparison of the results reveals that the LED has a strong nonlinear impact on the transmitted signal. Ignoring or considering this impact as ambient noise to design or optimize VLC systems is inaccurate.

5.4. Joint illumination and communication scenario validation

To evaluate the proposed LED model's applicability and accuracy in a realistic VLC system, a practical joint illumination and communication scenario validation is implemented. The central

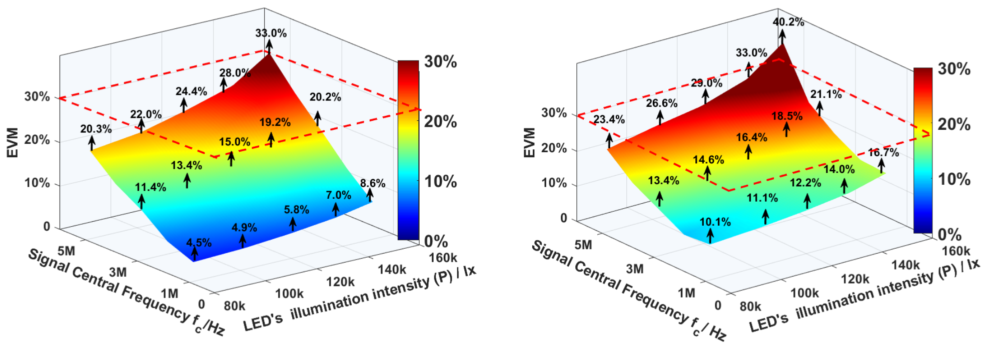

(a) (b)

Fig. 9. The EVM distribution of the VLC transmission when the input signal's central frequency and the LED's illumination intensity are varied. (a) Estimated by the proposed model. (b) Measured by the VLC system performance testbed.

frequency of the input signal is swept from 1MHz to 5MHz, and the bias voltage is set from 3.1V to 3.5V to generate the illumination intensity within 8×10^4 lx and 1.6×10^5 lx. It is measured closely against the LED. The EVM of the VLC transmission under various conditions is employed as an indicator of the VLC system performance. To clearly compare the measurement and emulation results, the gaps between test points are filled by interpolation forming the EVM distribution displayed in Fig. 9.

The results are discussed within the EVM range below 30% to guarantee communication quality. The results reveal a similar trend in both the estimated and measured EVM distribution under differing signal central frequencies and LED output illumination. Both the estimation and measurement substantiate that signal distortion worsens in proportion to the signal frequency and LED illumination intensity. Consequently, it is insufficient to investigate the communication performance of VLC systems in isolation. Joint illumination and communication LED model is necessary for a comprehensive evaluation of VLC systems.

Table 3. The error distribution between the measured and model estimated EVM

f_c/Hz Bias/V → P/lx	1MHz	2MHz	3MHz	4MHz	5MHz
3.1V→80.6klx	5.6%	2.7%	2.0%	2.4%	3.1%
3.2V→98.7klx	6.2%	3.0%	1.2%	2.0%	4.6%
3.3V→119.0klx	6.4%	2.9%	1.4%	0.6%	4.6%
3.4V→138.0klx	7.0%	4.0%	0.7%	0.1%	5.0%
3.5V→157.4klx	8.1%	3.1%	0.9%	0.3%	7.2%

The error of each test point between the estimated and measured values are depicted in Tab. 3, calculated as the measured EVM subtracted from the estimated EVM. The error distributes following the frequency characteristics. The error near 1MHz is significantly higher than those at other frequencies due to its proximity to the working boundary of the USRP. The error between 3MHz to 4MHz can be negligible when the LED's illumination intensity increases from low to high. It indicates the proposed model perfectly predicts the LED's nonlinear impact on VLC transmission with varied signal frequency and LED illumination intensity. Starting from 5MHz, both the measured and model-estimated EVM increase rapidly, in particular at high LED illumination intensity. The errors between them become meaningless once the EVM exceeds 30%. Although the disturbances coming from NLoS transmission, device thermal noise, and phosphor nonlinearity slightly influence the prediction results, the main nonlinear distortion of the VLC transmission caused by the LED is characterized by the proposed model.

6. Conclusion

This paper introduces a joint illumination and communication Gallium Nitride (GaN) Multiple Quantum Well (MQW) Light Emitting Diodes (LEDs) model tailored for Visible Light Communication (VLC) systems. The proposed model, grounded in the LED's physical properties, characterizes the inherent nonlinearity of the LED's electro-optic conversion. To facilitate real-world applications, the model is transformed into an equivalent circuit. The LED's signal response and output illumination intensity are derived and linked to the bias voltage. A commercial phosphor LED, possessing a structure akin to the theoretical model, is used as a sample LED for experimental validation, which is conducted to assess the applicability and accuracy of the proposed modeling methodology as well as the ability of the established model to accurately characterize the LED's nonlinear impact on VLC system performance.

The validation results confirm that the proposed model can accurately characterize the LED's nonlinearity and effectively predict its impact on the VLC system. Furthermore, both the experimental and model-based predictions indicate that the performance of the VLC system deteriorates as the LED's illumination intensity and the transmitted signal's frequency increase. This underscores the importance of our work, highlighting that a joint illumination and communication LED model is a critical tool for VLC system analysis and optimization.

The error analysis of the validation results illustrates future research directions. Initially, an investigation into the Non-Line-of-Sight (NLoS) VLC transmission model will aim to enhance channel estimation accuracy. This will be merged with the proposed LED model to predict system performance in a more intricate and realistic setting. Subsequently, a phosphor model will be developed to collaborate with the proposed model, thereby forming a complete LED lamp model. The lamp model will then be employed to investigate commercial scenarios of VLC systems.

Funding. The authors gratefully acknowledge the financial support of the Chinese Scholarship Council and the EU Horizon 2020 program towards the 6G BRAINS project H2020-ICT 101017226. This work was partly supported by the Young Natural Science Foundation of Jiangxi Province under Grant 20224BAB212004.

Disclosures. The authors declare no conflicts of interest.

Appendix I.

In quantum wells, the non-equilibrium electrons are degenerated and considered as 2DEG. A self-consistent approach [34] based on the Schrödinger equation and the Poisson equation in z direction is employed to derive the electrons concentration in quantum well expressed by Eq. (66) and (67). With the effective mass approximation, the step-like state density of electrons for each subband is determined by Eq. (68). The sheet charge density caused by polarization is calculated by Eq. (69).

$$\frac{1}{dz}(\epsilon_0\epsilon_q\frac{d\varphi_q(z)}{dz}) = -q(N_D^+(z) - n_q(z)) + \rho_s\delta(z - z_0) \tag{66}$$

$$-\frac{\hbar}{2m_\perp^*}\frac{d^2\Psi(z)}{dz^2} + q\varphi_q(z)\Psi(z) = E_n\Psi(z) \tag{67}$$

$$\sigma(E_n) = \frac{m_\perp^*}{\pi\hbar^2 L_q} \tag{68}$$

Table 4. Definition of Terms.

Terminology	Definition	Terminology	Definition
A	Ampere	$n_{c,q,b}$	Non-equilibrium carriers concentration of the layer
$A_{c,q,b}$	Transection area of each layer	n_0	Equilibrium minority concentration of the layer
A_{eff}	Effective area of barrier	N_D^+	Ionized donors density
A_{rec}	Area of photo-receiver	η	Ideal factor of diode
$\alpha_{1,2,3}$	Coefficient of the fitting curve ξ	η_L	Efficacy of LED
β_{sp}	Spontaneous emission coefficient	η_{ph}	Light extraction rate
C	Capacitance of each layer	P	Power
D	Distance between LED and VLC receiver	q	Elementary charge
γ_1	Coefficient of the SRH recombination	$\mathscr{R}_n$	Non-radiative recombination rate
γ_2	Coefficient of the radiative recombination	$\mathscr{R}_r$	Radiative recombination rate
γ_3	Coefficient of the Auger recombination	θ	Angle of receiving direction in VLC channel
E_{fn}	Quasi-Fermi level of electrons	R	Constant resistance
E_{fp}	Quasi-Fermi level of holes	r	Differential resistance
ϵ_0	Dielectric constant	ρ_s	Polarization charge density
ϵ_r	Relative dielectric constant	s	Photons density
φ	Potential energy in quantum well	σ	State density of electrons
$\Phi_{\frac{1}{2}}$	Semi-angle at half-power of LED	σ_n	Radom noise of VLC system
$\hbar$	Reduced Planck constant	T	Temperature
$I_{c,q,b}$	Current of each layer	τ_b	Effective space transport time
I_j	Injected current of LED	τ_{ph}	Photons lifetime
I_s	Reverse bias saturation current	V_D	Potential difference of barrier
k_B	Boltzmann constant	V_{ph}	Defined photon voltage
k	Wave number	V_{th}	Thermal voltage
κ	Sensitivity of APD	ψ	Angle of transmission direction in VLC channel
L	Thickness of the layer	Ψ	Wave function of electrons
m^*	Effective mass of electron	ω	Angular frequency
μ	Order of Lambertian radiation	Z	Impedance

$$\rho_s = P_{sp}(InGaN) + P_{pz}(InGaN) - P_{sp}(GaN) \tag{69}$$

In Poisson equation, it illustrates the relationship between the potential energy of electrons and the electrostatic charge distribution. $N_D^+(z)$ minus $n_q(z)$ represent the net charge of ionized donors and electrons in z direction. The impulse function $\delta(z - z_0)$ expresses the polarization charge ρ_s appeals only on the barrier surface z_0. In Schrödinger equation, it associates the electron energy with its potential. Respecting to the Fermi distribution, the sheet concentration of confined electrons in the x th subband is expressed as Eq. (70).

$$\begin{aligned} n_{iq}(z) &= \sum_x \int_0^\infty \sigma(E_n) f(E) dE (\Psi(z))^2 \\ &= \sum_x \frac{m_\perp^*}{\pi\hbar^2 L_q} \int_{E_x}^\infty \frac{dE}{1+\exp(\frac{E-E_{fn}}{k_B T})} (\Psi(z))^2 \\ &= \sum_x \frac{m_\perp^* k_B T}{\pi\hbar^2 L_q} ln(1+\exp(\frac{E_{fn}-E_x}{k_B T}))(\Psi(z))^2 \end{aligned} \tag{70}$$

For wurtzite material such as InGaN, the electron concentration at X and L valleys are negligible because their energy is much higher than the conduction band minimum located at Γ valley [51]. Thus the electron concentration in quantum wells is simplified as Eq. (71).

$$n_q = \frac{m^* k_B T}{\pi \hbar^2 L_q} \ln(1 + \exp(\frac{E_{fn} - E_{c1}}{k_B T})) \tag{71}$$

By setting the boundary of infinite potential well and calculating the coupled resolution of the Poisson equation and Schrödinger equation, the sheet concentration of confined electrons can be determined. Applying a self-consistent approach direct to a communication system analysis is too complete to implement. A polynomial fitting function ξ is employed to fit the energy between the electron quasi-Fermi level and the lowest conduction band E_{c1} shown in Eq. (72). The final simplified electron concentration in quantum wells is expressed by Eq. (74).

$$\begin{aligned} \xi(V_j) &= E_{fn}(V_j) - E_{c1}(V_j) \\ &= \alpha_1 V_j + \alpha_2 V_j^2 + \alpha_3 V_j^3 \end{aligned} \tag{72}$$

$$n^* = \frac{m^* k_B T}{\pi \hbar^2 L_q} \tag{73}$$

$$n_q(V_j) = n^* ln(1 + \exp(\frac{\xi(V_j)}{k_B T})) \tag{74}$$

References

1. H. Huang, H. Wu, C. Huang, Z. Chen, C. Wang, Z. Yang, and H. Wang, "Characteristics of micro-size light-emitting diode for illumination and visible light communication," Phys. Status Solidi (a) **215**, 1800484 (2018).
2. X. Huang, S. Chen, Z. Wang, J. Shi, Y. Wang, J. Xiao, and N. Chi, "2.0-gb/s visible light link based on adaptive bit allocation ofdm of a single phosphorescent white led," IEEE Photonics J. **7**, 1–8 (2015).
3. Y.-H. Chang, Y.-M. Huang, F.-J. Liou, C.-W. Chow, Y. Liu, H.-C. Kuo, C.-H. Yeh, W. H. Gunawan, T.-Y. Hung, and Y.-H. Jian, "2.805 gbit/s high-bandwidth phosphor white light visible light communication utilizing an ingan/gan semipolar blue micro-led," Opt. Express **30**, 16938–16946 (2022).
4. A. De Almeida, B. Santos, B. Paolo, and M. Quicheron, "Solid state lighting review–potential and challenges in europe," Renew. Sustain. Energy Rev. **34**, 30–48 (2014).
5. N. Chi, Y. Zhou, Y. Wei, and F. Hu, "Visible light communication in 6g: Advances, challenges, and prospects," IEEE Veh. Technol. Mag. **15**, 93–102 (2020).
6. D. Shi, X. Zhang, and L. Shi, "A joint backscatter and vlc-noma communication scheme for b5g/6g ummtc system," in *2021 IEEE International Symposium on Broadband Multimedia Systems and Broadcasting (BMSB),* (IEEE, 2021), pp. 1–4.
7. M. Božanić and S. Sinha, "Visible light communications for 6g," in *Mobile Communication Networks: 5G and a Vision of 6G,* (Springer, 2021), pp. 155–188.
8. S. Mumtaz, C. Jiang, A. Tölli, A. Al-Dulaimi, M. M. Butt, H. M. Asif, and M. I. Ashraf, "Guest editorial: 6g: The paradigm for future wireless communications," IEEE Wirel. Commun. **29**, 14–15 (2022).
9. P. Deng, M. Kavehrad, and M. A. Kashani, "Nonlinear modulation characteristics of white leds in visible light communications," in *Optical Fiber Communication Conference,* (Optica Publishing Group, 2015), pp. W2A–64.
10. H. Elgala, R. Mesleh, and H. Haas, "Non-linearity effects and predistortion in optical ofdm wireless transmission using leds," Int. J. Ultra Wideband Commun. Syst. **1**, 143–150 (2009).
11. K. Wang, Y. Liu, Z. Hong, and Z. Zeng, "Efficient timing offset estimation method tailored for aco-ofdm vlc systems," J. Light. Technol. **40**, 2307–2320 (2022).
12. G.-R. Lin, H.-C. Kuo, C.-H. Cheng, Y.-C. Wu, Y.-M. Huang, F.-J. Liou, and Y.-C. Lee, "Ultrafast 2× 2 green micro-led array for optical wireless communication beyond 5 gbit/s," Photonics Res. **9**, 2077–2087 (2021).
13. I. Stefan, H. Elgala, and H. Haas, "Study of dimming and led nonlinearity for aco-ofdm based vlc systems," in *2012 IEEE Wireless Communications and Networking Conference (WCNC),* (IEEE, 2012), pp. 990–994.
14. C. Chow, C. Yeh, Y. Liu, and Y. Liu, "Digital signal processing for light emitting diode based visible light communication," IEEE Photon. Soc. Newslett. **26**, 9–13 (2012).
15. H. Qian, S. Yao, S. Cai, and T. Zhou, "Adaptive postdistortion for nonlinear leds in visible light communications," IEEE Photonics J. **6**, 1–8 (2014).
16. A. Khalid, G. Cossu, R. Corsini, P. Choudhury, and E. Ciaramella, "1-gb/s transmission over a phosphorescent white led by using rate-adaptive discrete multitone modulation," IEEE Photonics J. **4**, 1465–1473 (2012).

17. S.-W. Wang, F. Chen, L. Liang, S. He, Y. Wang, X. Chen, and W. Lu, “A high-performance blue filter for a white-led-based visible light communication system,” IEEE Wirel. Commun. **22**, 61–67 (2015).
18. H. Elgala, R. Mesleh, and H. Haas, “A study of led nonlinearity effects on optical wireless transmission using ofdm,” in *2009 IFIP International Conference on Wireless and Optical Communications Networks,* (IEEE, 2009), pp. 1–5.
19. C. Yeh, C. W. Chow, Y. Liu, and P. Huang, “Simple digital fir equalizer design for improving the phosphor led modulation bandwidth in visible light communication,” Opt. Quantum Electron. **45**, 901–905 (2013).
20. Y. Qiu, H.-H. Chen, and W.-X. Meng, “Channel modeling for visible light communications—a survey,” Wirel. Commun. Mob. Comput. **16**, 2016–2034 (2016).
21. J.-Y. Sung, C.-W. Chow, and C.-H. Yeh, “Is blue optical filter necessary in high speed phosphor-based white light led visible light communications?” Opt. Express **22**, 20646–20651 (2014).
22. P.-C. Song, Z.-Y. Wu, X.-D. An, and J. Wang, “Energy efficiency analysis of light-emitting diodes with high modulation bandwidth,” IEEE Electron Device Lett. **42**, 1025–1028 (2021).
23. X. Li, Z. Ghassemlooy, S. Zvanovec, and L. N. Alves, “An equivalent circuit model of a commercial led with an esd protection component for vlc,” IEEE Photonics Technol. Lett. **33**, 777–779 (2021).
24. P. Salvador, J. Valls, J. L. Corral, V. Almenar, and M. J. Canet, “Linear response modeling of high luminous flux phosphor-coated white leds for vlc,” J. Light. Technol. **40**, 3761–3767 (2022).
25. X. Li, Z. Ghassemlooy, S. Zvanovec, M. Zhang, and A. Burton, “Equivalent circuit model of high power leds for vlc systems,” in *2019 2nd West Asian Colloquium on Optical Wireless Communications (WACOWC),* (IEEE, 2019), pp. 90–95.
26. X. Deng, M. Zhang, W. Pan, Z. Gao, J. Mo, C. Chen, X. Wu, X. Zou, L. Yan, and J.-P. Linnartz, “Physics-based led modeling and nonlinear distortion mitigating with real-time implementation,” IEEE Photonics J. **14**, 1–6 (2022).
27. X. Deng, K. Arulandu, Y. Wu, S. Mardanikorani, G. Zhou, and J.-P. M. Linnartz, “Modeling and analysis of transmitter performance in visible light communications,” IEEE Trans. on Veh. Technol. **68**, 2316–2331 (2019).
28. A. Alexeev, J.-P. M. Linnartz, K. Arulandu, and X. Deng, “Characterization of dynamic distortion in led light output for optical wireless communications,” Photonics Res. **9**, 916–928 (2021).
29. M.-H. Kim, M. F. Schubert, Q. Dai, J. K. Kim, E. F. Schubert, J. Piprek, and Y. Park, “Origin of efficiency droop in gan-based light-emitting diodes,” Appl. Phys. Lett. **91**, 183507 (2007).
30. H. Störmer, R. Dingle, A. Gossard, W. Wiegmann, and M. Sturge, “Two-dimensional electron gas at a semiconductor-semiconductor interface,” Solid State Commun. **29**, 705–709 (1979).
31. M. Burt, “The justification for applying the effective-mass approximation to microstructures,” J. Physics: Condens. Matter **4**, 6651 (1992).
32. N. Dutta, “Calculated threshold current of gaas quantum well lasers,” J. Appl. Phys. **53**, 7211–7214 (1982).
33. D. S. Gao, S. Kang, R. P. Bryan, and J. J. Coleman, “Modeling of quantum-well lasers for computer-aided analysis of optoelectronic integrated circuits,” IEEE J. Quantum Electron. **26**, 1206–1216 (1990).
34. B. Chouchen, A. El Aouami, M. H. Gazzah, A. Bajahzar, E. M. Feddi, F. Dujardin, and H. Belmabrouk, “Modeling the impact of temperature effect and polarization phenomenon on ingan/gan-multi-quantum well solar cells,” Optik **199**, 163385 (2019).
35. G. Rossi, R. Paoletti, and M. Meliga, “Spice simulation for analysis and design of fast 1.55 μm mqw laser diodes,” J. Light. Technol. **16**, 1509 (1998).
36. B. A. Ruzicka, L. K. Werake, H. Samassekou, and H. Zhao, “Ambipolar diffusion of photoexcited carriers in bulk gaas,” Appl. Phys. Lett. **97**, 262119 (2010).
37. L. V. Nguyen, A. J. Lowery, P. C. Gurney, and D. Novak, “A time-domain model for high-speed quantum-well lasers including carrier transport effects,” IEEE J. Sel. Top. Quantum Electron. **1**, 494–504 (1995).
38. W. Shockley, “The theory of p-n junctions in semiconductors and p-n junction transistors,” Bell Syst. Tech. J. **28**, 435–489 (1949).
39. R. Nagarajan, M. Ishikawa, T. Fukushima, R. S. Geels, and J. E. Bowers, “High speed quantum-well lasers and carrier transport effects,” IEEE J. Quantum Electron. **28**, 1990–2008 (1992).
40. F. Olivier, A. Daami, C. Licitra, and F. Templier, “Shockley-read-hall and auger non-radiative recombination in gan based leds: A size effect study,” Appl. Phys. Lett. **111**, 022104 (2017).
41. K. Seeger, *Semiconductor physics* (Springer Science & Business Media, 2013).
42. S. Vappangi and V. Mani, “Performance analysis of dst-based intensity modulated/direct detection (im/dd) systems for vlc,” IEEE Sensors J. **19**, 1320–1337 (2018).
43. G. He and L. Zheng, “A model for led spectra at different drive currents,” Chin. Opt. Lett. **8**, 1090–1094 (2010).
44. E. Mechtly, *The international system of units: physical constants and conversion factors*, vol. 7012 (Scientific and Technical Information Division, National Aeronautics and Space Administration, 1964).
45. J. C. Campbell, S. Demiguel, F. Ma, A. Beck, X. Guo, S. Wang, X. Zheng, X. Li, J. D. Beck, M. A. Kinch *et al.*, “Recent advances in avalanche photodiodes,” IEEE J. Sel. Top. Quantum Electron. **10**, 777–787 (2004).
46. Epistar, “leddatasheet,” https://www.epistar.com/Upload/Led/ES-VABCF45G.pdf.
47. U. K. Mishra and J. Singh, *Semiconductor device physics and design*, vol. 83 (Springer, 2008).
48. L. Shi, D. Shi, X. Zhang, B. Meunier, H. Zhang, Z. Wang, A. Vladimirescu, W. Li, Y. Zhang, J. Cosmas *et al.*, “5g internet of radio light positioning system for indoor broadcasting service,” IEEE Trans. on Broadcast. **66**, 534–544 (2020).
49. V. Jungnickel, M. Uysal, N. Serafimovski, T. Baykas, D. O’Brien, E. Ciaramella, Z. Ghassemlooy, R. Green, H. Haas,

P. A. Haigh *et al.*, "A european view on the next generation optical wireless communication standard," in *2015 IEEE Conference on Standards for Communications and Networking (CSCN),* (IEEE, 2015), pp. 106–111.

50. A. Ahaitouf, H. Srour, S. O. S. Hamady, N. Fressengeas, A. Ougazzaden, and J.-P. Salvestrini, "Interface state effects in gan schottky diodes," Thin Solid Films **522**, 345–351 (2012).
51. M. Cardona, "Band parameters of semiconductors with zincblende, wurtzite, and germanium structure," J. Phys. Chem. Solids **24**, 1543–1555 (1963).